Antiferromagnetic structures and electronic energy levels at reconstructed NiO(111) surfaces: A DFT + U study

Lesheng Li and Yosuke Kanai*
Department of Chemistry, University of North Carolina at Chapel Hill, North Carolina 27599-3290, USA
(Received 29 April 2015; revised manuscript received 11 May 2015; published 3 June 2015)

We studied how the surface reconstruction and passivation influence the antiferromagnetic and electronic structures of NiO(111) surface using first-principles electronic structure calculations. These features lead to a surprisingly wide variety of different surface electronic structures, and some surfaces are even metallic. Different reconstructions and surface passivation were also found to qualitatively alter the charge-transfer band gap type of bulk NiO. At the same time, the antiferromagnetic character of bulk NiO in the ⟨111⟩ direction is retained even near the surface, and the magnetic moment quickly converges to the bulk value within a few surface layers.

DOI: 10.1103/PhysRevB.91.235304 PACS number(s): 73.20.−r

I. INTRODUCTION

Nickel oxide (NiO) has attracted considerable attention for decades because it offers a number of desirable magnetic and electronic properties such as antiferromagnetism and p-type semiconducting character, respectively, for potential technological applications. In recent years, NiO nanomaterials have been widely investigated for various technological applications including catalysis, battery cathodes, gas sensors, electrochromic films, and solar cells [1–6], and therefore it has become important to understand how material surfaces alter these magnetic and electronic properties of NiO.

An important characteristic of bulk NiO is its antiferromagnetic (AFM) character in the [111] direction. NiO has attracted great attention because of its high Néel temperature of 523 K [7]. Small particles of an AFM material start to behave differently from their bulk counterpart by exhibiting a variety of new physical phenomena, such as superparamagnetism and weak ferromagnetism as discussed by Néel [8]. Within the Néel's model, the large permanent magnetic moments in nanomaterials are attributed to uncompensated spins, and the common two-sublattice model of the antiferromagetic ordering is still applicable. However, the two-sublattice model does not fully explain the experimentally observed anomalous magnetic properties of NiO nanoparticles [9], such as large magnetic moments, enhanced coercivity, and hysteresis loop shifts. Kodama and coworkers instead proposed a multisublattice model [9] to explain the large magnetic moment. In their study, numerical modeling of spin configurations in NiO nanoparticles suggested a new finite-size effect, where the reduced coordination of surface spins causes a fundamental change in the magnetic order throughout the particle, by creating multisublattice (eight-, six-, or four-sublattice) spin ordering. Recently, several studies [9–14] have shown that NiO nanoparticles would be formed by a spin-glass-like shell strongly coupled to an AFM core. Such a unique magnetic structure leads to the exchange bias (EB) phenomenon [12,15], which can be attributed to the enhanced coercivity and loop shift. Indeed, a breakdown of the antiferromagnetic order has been suggested near the top layers for some structures, where an uncompensated FM or a spin-glass-like surface shell is exchange coupled to an AFM core [15]. In addition, surface morphology was proposed to control magnetic properties such as disappearance of the AFM core and the variation of the EB field and coercivity in small NiO nanoparticles [14]. However, existing studies on NiO nanoparticles mainly focus on size effects on the magnetism of the system. The surface morphology aspect needs to be investigated in detail.

NiO materials have attracted significant interests also for solar energy conversion because of their p-type character. In the context of solar cells, many groups have started to explore p-type semiconductors for dye-sensitized solar cells (DSSCs) [16–18] and dye-sensitized photoelectrosynthesis cells (DSPECs) [19,20] where hole injection from an adsorbed molecule into the valence band of the surface takes place [21–23] instead of the electron injection as in the traditional n-type system. The motivation for developing a complementary p-type system stems from building a desirable tandem cell composed of both photoanode and photocathode materials [24,25], which has the capability of surpassing the Shockley-Queisser limit [26,27]. Mesoporous NiO interfaced with an organic dye has been studied [28,29] and shown to achieve the photoconversion efficiency of 1.3% in context of p-type DSSC in recent years [28]. However, this device exhibits low power-conversion efficiencies in p-DSSCs devices, which has been interpreted as a consequence of several reasons, including small open circuit voltage (V_{OC}), low hole mobility, poor chromophore surface loading, and high charge carrier recombination rates [30,31]. By synthesizing the nanoplatelets with the (111) surface exposed, Flynn and coworkers have recently investigated the p-DSSC performance and its dependence on various annealing conditions for the synthesis [32]. These nanoplatelets are less than 10 nm in thickness in the [111] direction, and the observed dependence of various optical and electrical properties on the synthesis condition suggest a high degree of morphological changes. Given the dominating (111) surfaces of the nanoplatelets, varying electronic properties of the surface could potentially explain the observed dependence on the synthesis condition. Their work demonstrated that the power conversion efficiency depends strongly on the annealing temperature of the material because hole mobility, surface morphology, as well as the hole injection efficiency are influenced strongly by atomistic details of the nanomaterials.

*Author to whom correspondence should be addressed: ykanai@unc.edu

Experimental observations suggest that the electronic structure at the NiO(111) surface depends significantly on the surface reconstruction, and the antiferromagnetic order could also be strongly affected at the surface as well. Various types of reconstructions and surface passivation have been reported both experimentally and theoretically for the NiO(111) surface. In particular, so-called octopolar, $2\times2-\alpha$, and Rt3 appear to be stable reconstruction phases of the (111) surface [33–43]. Furthermore, hydrogenated and hydroxylated surfaces have been recently characterized in experiments using STM and THEED [38,39,44]. Despite the potential importance of these reconstructions at the NiO(111) surface for material properties, especially for NiO nanomaterials, a comprehensive investigation on how the reconstructions and experimentally common surface passivation of hydrogenation/hydroxylation affect the surface electronic structure and magnetization is yet to be reported in literature. We present here an exhaustive theoretical investigation of this aspect of the rich field of the NiO(111) surface.

II. THEORETICAL METHOD

A. Hubbard-U correction

Density functional theory (DFT) calculations were performed with the Hubbard correction using QUANTUM ESPRESSO code [45]. The interaction of the valence electrons with ionic cores was described by ultrasoft pseudopotentials, and the Kohn-Sham orbitals were represented in a plane-wave basis set, where the energy cutoff of plane wave and the density cutoff were 30 Ry and 300 Ry, respectively. All important convergence parameters have been monitored to achieve an overall accuracy of 1×10^{-6} eV. The surface Brillouin zone integration was performed with a $4\times4\times1$ Monkhorst-Pack [46] k-point grids. Spin-polarized calculations were carried out in this present work because of the antiferromagnetic nature of both bulk NiO and NiO(111) surfaces.

First-principles modeling of systems with localized d states such as the systems studied in our work is currently a great challenge in condensed-matter physics. DFT in the standard local-density approximation (LDA) or generalized gradient approximation (GGA) proves to be problematic, which is best illustrated in the well-known failure of LDA/GGA for later transition metal oxides [47]. A simple and effective approach to overcome the major failure of DFT is the DFT + U method in which the DFT total energy is augmented by a local Hubbard correction, characterized by the on-site Coulomb interaction U [48–51]. In our present study, Hubbard-U correction approach was applied to the generalized-gradient approximation (GGA) of Perdew, Burke, and Ernzerhof (PBE) [52] because of the strong electron correlation of the partially filled d shells in Ni atoms. In practical DFT + U calculations, Hubbard parameter U and exchange parameter J are not considered separately, but are often combined by redefining U_{eff} as their difference $U_{\text{eff}} = U - J$ and setting $J = 0$ [53]. We therefore employ the same strategy to use U_{eff} with $J = 0$ during our calculations. Anisimov, Zaanen, and Andersen previously determined the effective Hubbard parameter of NiO to be 7.1 eV using linear muffin-tin-orbital method in the atomic-sphere-approximation-based constrained DFT calculations [48]. Although this value has been widely applied [54], several theoretical studies have shown that this value leads to inconsistent antiferromagnetic moment and optical properties as measured in experiments [53,55,56]. Also, significantly smaller Hubbard-U values are found in theoretical works based on the linear-response approach [51,57] and constrained random-phase approximation (RPA) [58,59].

In order to illustrate how essential it is to employ the Hubbard-U correction, we present the projected density of states (PDOS) obtained from GGA and GGA + U (U parameter as 5.4 and 8.0 eV) calculations for bulk NiO in Fig. 8 (see Appendix A). Figure 8 shows that the Hubbard-U correction increases the band gap dramatically from 1.49–3.38 eV as the U parameter varies from 0 (DFT calculation without Hubbard-U correction) to 8.0 eV. Another important feature to be noticed in the PDOS depicted in Fig. 8 is the fact that GGA + U qualitatively modifies the nature of the states at the top of the valence band, and hence the nature of the band gap: in the GGA calculations the top of valence band is mainly dominated by Ni-3d electrons; on the other hand, in the GGA + U calculations the O-2p electrons give the most important contribution to the top of valence band. Both GGA and GGA + U indicate that the bottom of the conduction band is mostly contributed by Ni-3d states. Thus, the enhancement of the O-2p character near the top of valence band leads to the change of the insulating band gap character from Mott-Hubbard type based on GGA calculations to charge-transfer type [60] according to GGA + U calculations, which agrees well with the findings in previous works, both experimentally and theoretically [51,54–56,61–65]. Although our calculation using the linear response approach [51,57] gives 4.45 eV for the value of U, we used the value of 5.4 eV in this work so that our work can be compared to previous theoretical works that use 5.4 eV for the U value [37,42,56,66,67]. We observe that our choice of 4.45 eV or 5.4 eV for the U parameter does not significantly influence the electronic structure including the magnetic moment and energy gap type.

B. Surface structures

The ideal 1×1 surface structure as well as three prominent surface reconstruction models of octopolar, $2\times2-\alpha$, and Rt3 were considered in this present work because of their stability [33–39]. The top view of the supercell structures is shown in Fig. 1, and the side view can be found in Appendix B (Fig. 9). Because the oxygen-terminated surface has shown to be more stable than the metal-terminated surface for MgO with the $2\times2-\alpha$ reconstruction [38,68] and also the calculated phase diagrams are nearly identical for MgO and NiO surface [39], we consider here only the oxygen-terminated surface of the $2\times2-\alpha$ reconstruction. In addition, both Ni-terminated and O-terminated Rt3 reconstructions were considered as suggested by Ciston *et al.* [38]. These two surfaces are actually both oxygen terminated at the atomistic level although we follow here the original naming scheme. Hydroxylation/hydrogenation as recently characterized in STM and THEED studies [38,39,44] were modeled by attaching hydrogen atoms on the surface of O-terminated and Ni-terminated surface, respectively. For simplicity, we use several shorthand notations throughout the following discussions. For

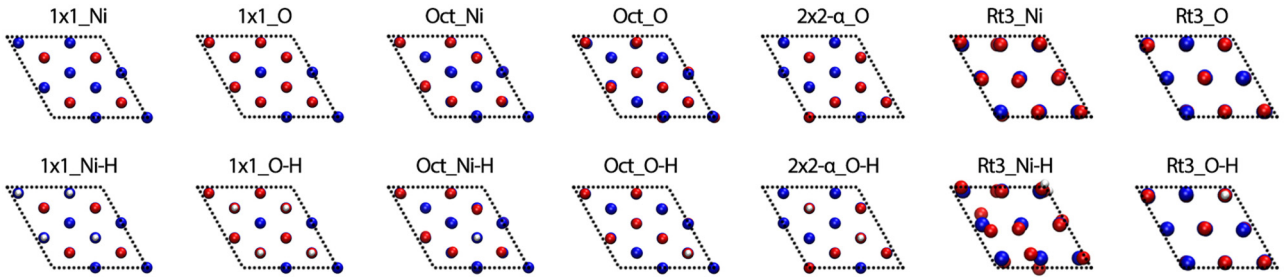

FIG. 1. (Color online) Top view of the super cells used in our calculations for 1×1_Ni, 1×1_O, Oct_Ni, Oct_O, 2×2-α_O, Rt3_Ni, and Rt3_O surface models, and their corresponding hydrogenated/hydroxylated surfaces. Red and blue balls represent oxygen and nickel atoms, and hydrogen atoms are shown in white.

example, Oct_O and Oct_Ni refer to octopolar NiO(111) surface terminated by oxygen and nickel atoms, respectively. Oct_O-H and Oct_Ni-H refer to hydroxylated Oct_O and hydrogenated Oct_Ni surfaces.

In our calculations, all the surfaces are modeled by periodically repeating symmetric slabs. The vacuum region between the repeated slabs is set to 15 Å, so the interaction between repeating slabs in the vacuum direction is negligible. In order to explore how thick the slabs need to be for obtaining well-converged results for both magnetic and electronic properties of the surface, slabs containing six, eight, and ten layers of Ni with thickness ranging from 1.18–2.41 nm were calculated in our work, and the results are summarized in Table II. The relevant surface properties of interest here are well converged with respect to the thickness of the slab even with six layers. Hence, the results from the six-layer slabs are discussed for the reminder of the work.

III. RESULTS AND DISCUSSION

A. Antiferromagnetic ordering

The intrinsic antiferromagnetic nature of NiO can be characterized by the magnetization density (spin density) defined as $m(r) = \rho_{\uparrow}(r) - \rho_{\downarrow}(r)$, where $\rho_{\uparrow}(r)$ and $\rho_{\downarrow}(r)$ are the electronic density for spin-up and spin-down electrons, respectively. Spin polarization (magnetization) of nickel atoms changes from one layer to the next alternatively along [111] direction. There exist three different types of atoms based on the magnetization density. Nickel atoms can be distinguished according to the localization of spin-up $|\psi_{\uparrow}\rangle$ and spin-down $|\psi_{\downarrow}\rangle$ states, and oxygen atoms are essentially all spin unpolarized for bulk NiO.

1. *Ideal* 1×1 *and octopolar reconstructed surfaces*

The magnetization density for the ideal 1×1 and octopolar surface is shown in Fig. 2. The alternatively distributed yellow and purple isosurfaces, representing spin-up and spin-down density, indicate that ideal 1×1 and octopolar reconstructed surface retain the same antiferromagnetic character as in bulk NiO (see Appendix C, Fig. 10). The calculated magnetic moments are summarized in Table I for each layer. The bulk value of the magnetic moment for Ni is $\pm 1.59\,\mu_B$, and both ideal 1×1 and octopolar surfaces show that the magnetic moment rapidly converges to the bulk NiO value, already at the second Ni layer as shown in Table I. At the same time, small spin polarization is observed for the oxygen layers.

2. *2×2 − α reconstructed surfaces*

Figure 2 also shows the magnetization density for 2×2_α-O and 2×2_α-O-H reconstructed surfaces. Although the spin-up and spin-down densities are alternatively distributed for Ni layers in the 2×2_α-O as for the 1×1 and octopolar reconstructed surfaces, significant magnetization is observed for the top surface oxygen layer. The magnetic moment of the top oxygen layer is as high as $0.81\,\mu_B$, exhibiting a qualitative different behavior from those oxygen layers in bulk NiO. On the other hand, the hydroxylated surface, 2×2_α-O-H, shows the same magnetic pattern exhibited for the ideal 1×1 and octopolar reconstructed surfaces. As shown in Table I, the magnetic moment for the Ni layers converges quickly to the bulk NiO value, already at the first Ni layer (S-1 layer) for both clean and hydroxylated surfaces.

3. *Rt3 reconstructed surfaces*

Figure 2 also shows the magnetization density of Rt3 reconstructed surfaces. In addition to the alternatively distribution of the spin-up and spin-down densities for the Ni layers, a significant magnetization of the top oxygen surface layer (S layer) is observed for the Rt3_Ni reconstructed surface. Interestingly, for the hydrogenated surface, Rt3_Ni-H, the magnetization essentially disappears for the first Ni layer (S-1 layer). The magnetic moment is as large as $1.65\,\mu_B$ for the S layer of oxygen atoms in the Rt3_Ni surface, and the magnetic moment for the S-1 layer of Ni atoms is only $-0.08\,\mu_B$ in the Rt3_Ni-H surface. Unlike the Rt3_Ni reconstructed surface, the Rt3_O reconstructed surface shows the same antiferromagnetic ordering in both clean and hydroxylated surfaces. As can be seen in Table I, the magnetic moments for this Rt3_O surface are quite close to those of ideal 1×1 and octopolar reconstructed surfaces. The magnetic moment of the Ni layers also converges rapidly to the bulk NiO value, and oxygen layers exhibit negligible spin polarization.

As discussed in the Introduction, the breakdown of the antiferromagnetic order near the top surface layers have been discussed in the literature for small particles, inhomogeneous materials, coated antiferromagnetic single crystals, and thin films [15]. They show that uncompensated ferromagnetic (FM) or a spin-glass-like surface shell is exchange coupled to an AFM core. Such a breakdown of the AFM order and

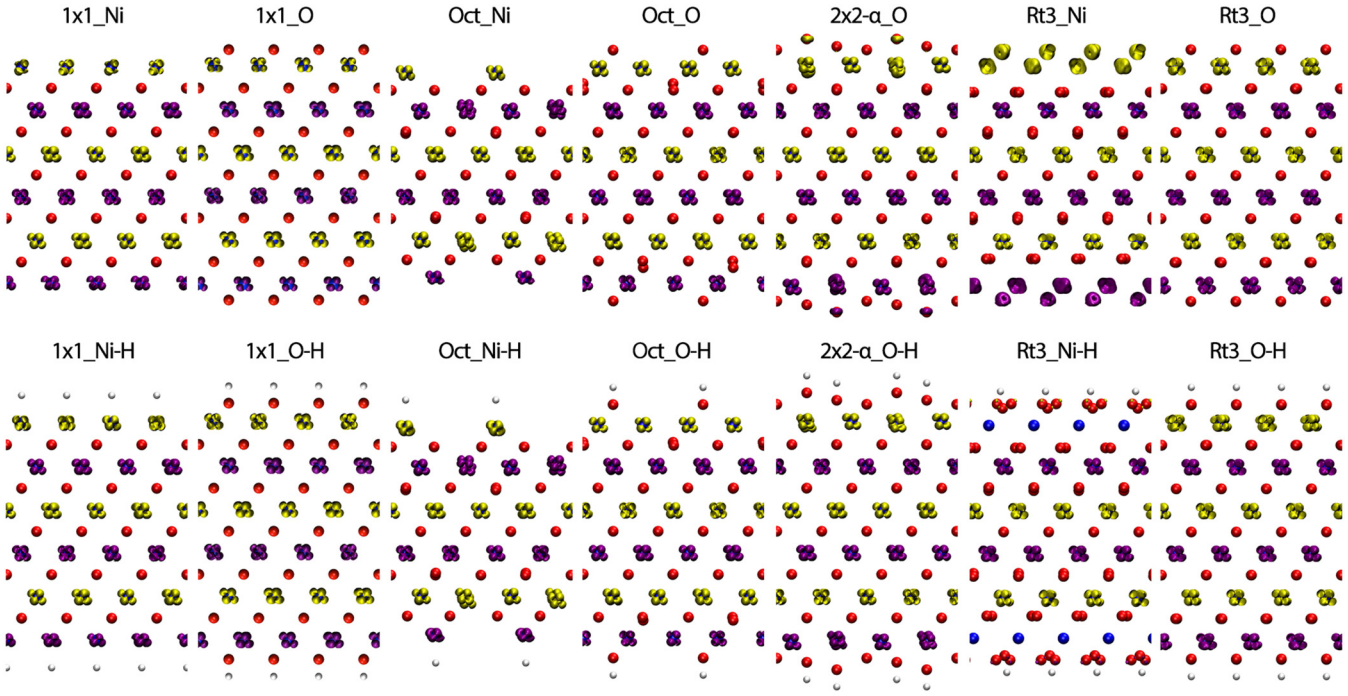

FIG. 2. (Color online) Side view of the magnetization density $m(x) = \rho_{\uparrow}(x) - \rho_{\downarrow}(x)$ for 1×1_Ni, 1×1_O, Oct_Ni, Oct_O, 2×2-α_O, Rt3_Ni, and Rt3_O surface models, as well as their corresponding hydrogenated/hydroxylated surfaces. The top halves are clean surfaces and the bottom halves are passivated surfaces. Yellow and purple isosurface indicate spin-up and spin-down density, respectively. Red and blue balls represent oxygen and nickel atoms, and hydrogen atoms are shown in white.

the corresponding core-shell magnetic structure have been interpreted and modeled as a finite-size effect of nanoparticles [9–14]. At the same time, our atomistic calculations here show that surface reconstruction and hydroxylation/hydrogenation play an equally important role in determining the magnetic properties at the NiO(111) surface. The NiO(111) surface exhibits a surprisingly wide variation in the magnetic behavior, depending on not only the reconstruction type and surface terminations but also on the hydroxylation/hydrogenation, which is an important factor in experiments. At the same time, the antiferromagnetic behavior of bulk NiO is recovered quickly away from the top surface layer in all cases. Our calculations show that the magnetic moment effectively converges to the bulk value, already at the second Ni layer. These results indicate that the antiferromagnetic behavior is likely to be retained internally in the nanoplatelets structures of several nm thickness [32] regardless of the surface structure, which remains unresolved.

TABLE I. Calculated magnetic moment for different surface structures. *S*: surface layer; *S-N*: the *N*th layer below top surface. Only the values for the top half slab are listed due to the symmetry. The atom type of the surface layer is indicated in the bracket.

		Magnetic Moment/μ_B						
Structures		*S*	*S*-1	*S*-2	*S*-3	*S*-4	*S*-5	*S*-6
1×1_Ni	Clean	1.08 (Ni)	−0.05	−1.60	0.00	1.60	0.00	N/A
	Hydrogenated	1.46 (Ni)	0.05	−1.60	0.00	1.60	0.00	N/A
1×1_O	Clean	0.32 (O)	−1.18	0.06	1.59	0.00	−1.60	0.00
	Hydroxylated	−0.14 (O)	−1.64	0.00	1.60	0.00	−1.60	0.00
Oct_Ni	Clean	1.57 (Ni)	−0.10	−1.61	0.00	1.60	0.00	N/A
	Hydrogenated	1.75 (Ni)	0.00	−1.61	0.01	1.60	0.00	N/A
Oct_O	Clean	0.22 (O)	1.61	0.02	−1.60	0.00	1.60	0.00
	Hydroxylated	0.06 (O)	1.39	0.00	−1.60	0.00	1.60	0.00
2×2-α_O	Clean	0.81 (O)	1.60	0.07	−1.60	0.01	1.60	0.00
	Hydroxylated	0.23 (O)	1.60	0.01	−1.60	0.01	1.60	0.00
Rt3_Ni	Clean	1.65 (O)	1.72	0.29	−1.36	0.06	1.59	0.00
	Hydrogenated	0.15 (O)	−0.08	0.11	−1.40	0.06	1.59	0.00
Rt3_O	Clean	−0.02 (O)	1.47	−0.01	−1.60	0.00	1.60	0.00
	Hydroxylated	0.25 (O)	1.61	0.01	−1.60	0.00	1.60	0.00

B. Density of states

In addition to the antiferromagnetic order at the reconstructed surfaces, the surface electronic structure is quite important because of a growing interest in NiO as a promising p-type material. In order to analyze the surface-induced changes in the electronic structure, we discuss here the projection of the density of states on Ni-3d and O-2p orbitals from each layer (layer-resolved PDOS). We align the bulk NiO density of states to the PDOS of the innermost layer of the NiO slabs used in the calculations since the surface electronic structure quickly converges to that of bulk for all these reconstructed surfaces as seen by the convergence of the magnetic moment (Table I).

1. *Ideal* 1×1 *surfaces*

The layer-resolved PDOS for ideal 1×1_Ni and 1×1_Ni-H surfaces is shown in Figs. 3(a) and 3(b), respectively. Note that different scales are used in the Y axis for the Ni-3d layers (blue) and for the O-2p layers (red). The PDOS from the top half of the surface slab is shown here because of the inversion symmetry of the surface slab in the calculation. The valence band maximum (VBM) of bulk NiO is set to be the reference energy of zero, and the dashed line indicates Fermi level of the surface. As shown in Figs. 3(a) and 3(b), the PDOS of the inner layers matches quite well with the DOS of bulk NiO (depicted in shaded gray area). At the same time, the PDOS changes dramatically for the top few layers. Significant changes in Ni-3d (S layer) and O-2p state (S-1 layer) cause the surface to be metallic for both 1×1_Ni and 1×1_Ni-H surfaces.

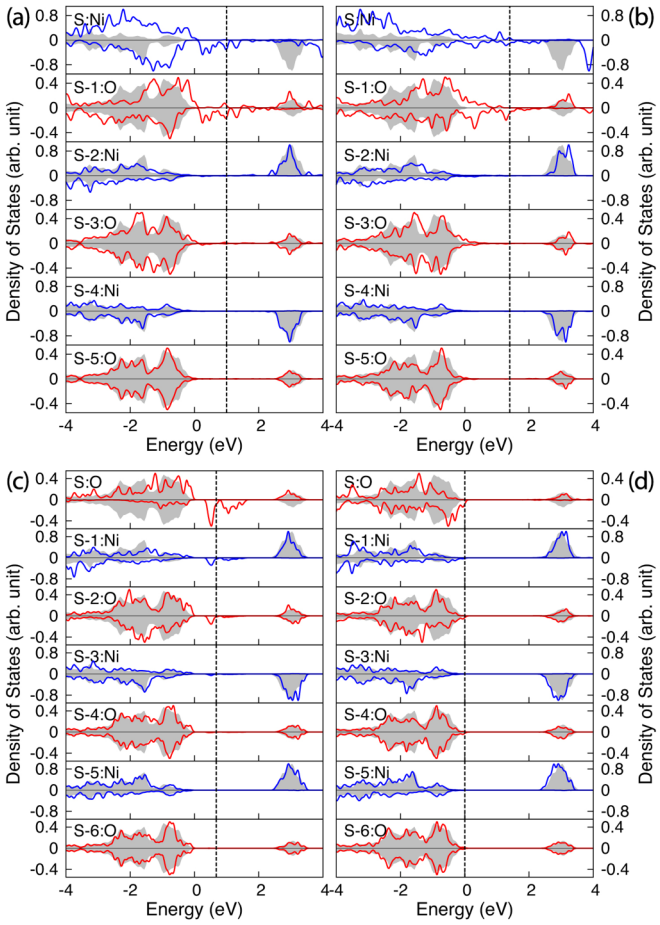

FIG. 3. (Color online) Layer-resolved PDOS comparison between bulk NiO and (a) 1×1_Ni, (b) 1×1_Ni-H, (c) 1×1_O, (d) 1×1_O-H surface structures. VBM of bulk NiO is set to 0, Fermi levels of different reconstructed surfaces are shown in dashed line. The Ni-3d and O-2p PDOS are represented by blue and red lines, and the bulk NiO PDOS is shown in solid gray.

Similarly, layer-resolved PDOS for 1×1_O and 1×1_O-H is shown in Figs. 3(c) and 3(d). Similar to Ni termination, 1×1_O surface shows a metallic surface again due to the enhancement of Ni-3d and O-2p state within the bulk band gap energy range for the top layers. At the same time, the hydroxylated surface with hydrogen atoms, Ni-3d, and O-2p state are enhanced only near the VBM and conduction band minimum (CBM) of bulk NiO. Note that here we only show the contribution from O-2p and Ni-3d orbitals in the layer-resolved PDOS figure, but the contribution from s orbitals is not shown. 1×1_O-H surface shows an insulating energy gap of 1.8 eV, where VBM and CBM mainly stem from O-2p states in the S layer and hydrogen s orbitals.

Figure 3 shows that prominent changes in the electronic structure at the surface come primarily from the top few layers, and this is also the case for other surfaces that are discussed in the following section. This also explains the fast convergence of the electronic/magnetic properties with respect to the slab thickness in our calculations as discussed above in Sec. II.

2. *Octopolar reconstructed surfaces*

The layer-resolved PDOS for Oct_Ni surface is shown in Fig. 4(a). The surface VBM mostly originates from the oxygen atoms in the S-1 layer, mainly of O-2p orbitals. On the other hand, the surface CBM derives significantly from the nickel atoms in S-2 layer, mainly of Ni-3d orbitals. Consequently, a charge-transfer-type energy gap is developed at the Oct_Ni surface with the surface energy gap of 1.25 eV. The effect of hydrogenation at the surface, Oct_Ni-H, is shown in Fig. 4(b). Distinct surface states appear within the bulk band gap, and the surface VBM is contributed almost equally from S layer (Ni-3d character) and S-1 layer (O-2p character) while the surface CBM is predominantly from Ni-3d states of S layer. This energy gap character of a hybrid type as described by the Zaanen-Sawatzky-Allen model [69] agrees well with previous mixture type proposed by Schuler and coworkers [70] and the surface energy gap is only 0.41 eV for Oct_Ni-H surface.

For the Oct_O surfaces shown in Fig. 4(c), the VBM derives significantly from O-2p states in S-2 layer. On the other hand, CBM originates mostly from the Ni atoms in S-1 layer, mainly of Ni-3d orbitals. Consequently, the insulating energy gap is of charge-transfer type with a gap of 1.18 eV. The layer-resolved PDOS for the hydrogenated Oct_O-H surface is shown in Fig. 4(d). The surface electronic structure changes dramatically from that of the clean Oct_O surface. New surface states appear within the bulk band gap. The new surface-induced occupied states stem mostly from subsurfaces, S-1 layer (Ni-3d character). The nickel atoms in S-1 layer give rise to the new unoccupied states of Ni-3d character,

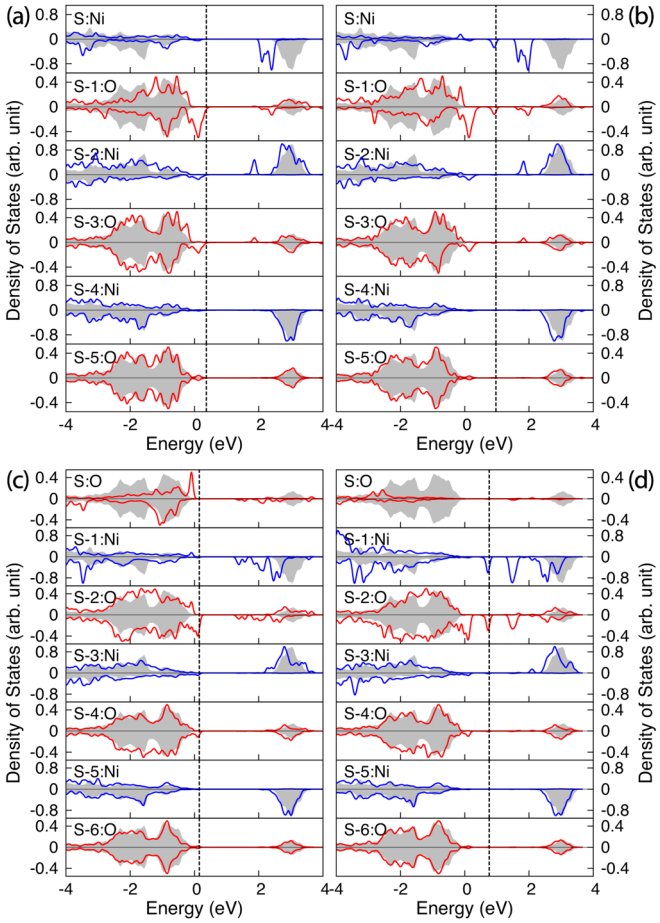

FIG. 4. (Color online) Layer-resolved PDOS comparison between bulk NiO and (a) Oct_Ni, (b) Oct_Ni-H, (c) Oct_O, (d) Oct_O-H surface structures. VBM of bulk NiO is set to 0, Fermi levels of different reconstructed surfaces are shown in dashed line. The Ni-3d and O-2p PDOS are represented by blue and red lines, and the bulk NiO PDOS is shown in solid gray.

resulting in a Mott-type energy gap (3d - 3d) rather than the charge-transfer type of Oct_O surface or bulk NiO. The energy gap at surface is only 0.53 eV for this Oct_O-H surface. Importantly, for both Oct_O and Oct_O-H surface, the new surface states in the bulk band gap derive from the subsurface layers and not from the topmost layer of these surfaces.

3. 2×2-α reconstructed surfaces

In the case of the 2×2-α_O as shown in Fig. 5(a), surface states are also localized on the top few layers. There are significant changes within the bulk band gap, and the energy gap at surface is only 0.24 eV. The surface VBM and CBM derived mainly from O-2p states in the topmost layer (S), making it the insulating gap with O2p-O2p type. For the hydroxylated surface of 2×2-α_O-H as shown in Fig. 5(b), the surface electronic structure is quite different from that of clean 2×2-α_O surface. Surface states appear within the bulk band gap only near the VBM and CBM, and the energy gap at this surface is 1.7 eV. For this 2×2-α_O-H, we found the insulating gap to be of the charge-transfer type, because the

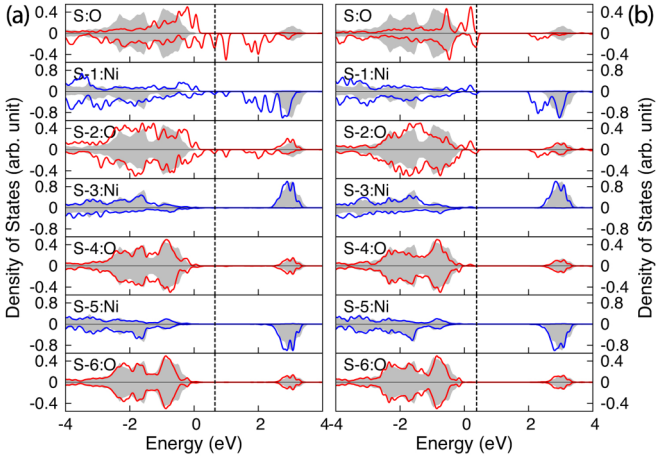

FIG. 5. (Color online) Layer-resolved PDOS of 2×2-α_O and 2×2-α_O-H surface structure and bulk NiO, VBM of bulk NiO is set to 0, Fermi levels of different reconstructed surfaces are shown in dashed line. The Ni-3d and O-2p PDOS are represented by blue and red lines, and the bulk NiO PDOS is shown in solid gray.

surface VBM and CBM stem mostly from the topmost S layer of O-2p states and the S-1 layer of Ni-3d states, respectively.

4. Rt3 reconstructed surfaces

Layer-resolved PDOS for the Rt3_Ni and Rt3_Ni-H surfaces are shown in Figs. 6(a) and 6(b), respectively. The most obvious change is that both clean and hydrogenated Rt3_Ni reconstructed surfaces exhibit metallic surfaces. There is significant enhancement of contributions from Ni-3d and O-2p states near the Fermi level in the top few surface layers.

Figures 6(c) and 6(d) show the layer-resolved PDOS of Rt3_O and Rt3_O-H surfaces, respectively. As in the case of the Rt3_O surface, it is metallic in character, resulting from the enhanced contributions near the Fermi energy from Ni-3d and O-2p states on the top surface layers. However, when the hydroxylated layer is formed, Ni-3d and O-2p states are enhanced near the band edges of bulk NiO. This yields the energy gap of 1.37 eV at surface. The surface VBM and CBM mostly derive from S layer of O-2p orbitals and S-1 layer of Ni-3d character, respectively, making it a charge-transfer-type gap.

As discussed in the Introduction section, NiO is widely considered as a promising p-type material for a wide range of energy conversion devices. For technological applications such as p−DSSCs [16–18] and p−DSPECs [19,20], understanding how the reconstruction at the NiO(111) surface alters the alignment of the energy levels is important for designing a heterojunction interface with photon-absorbing molecular systems. In this context, the relative position of the electronic energy levels (especially the VBM and CBM) with respect to the vacuum level or the normal hydrogen electrode (NHE) is a key criterion for optimizing the interface for higher efficiency. Figure 7 shows the energy levels alignment for all the reconstructed surfaces that are considered in this work. Kohn-Sham eigenvalues are aligned with respect to the vacuum level by calculating the plane-averaged electrostatic potential in the normal direction of the surface. We find that

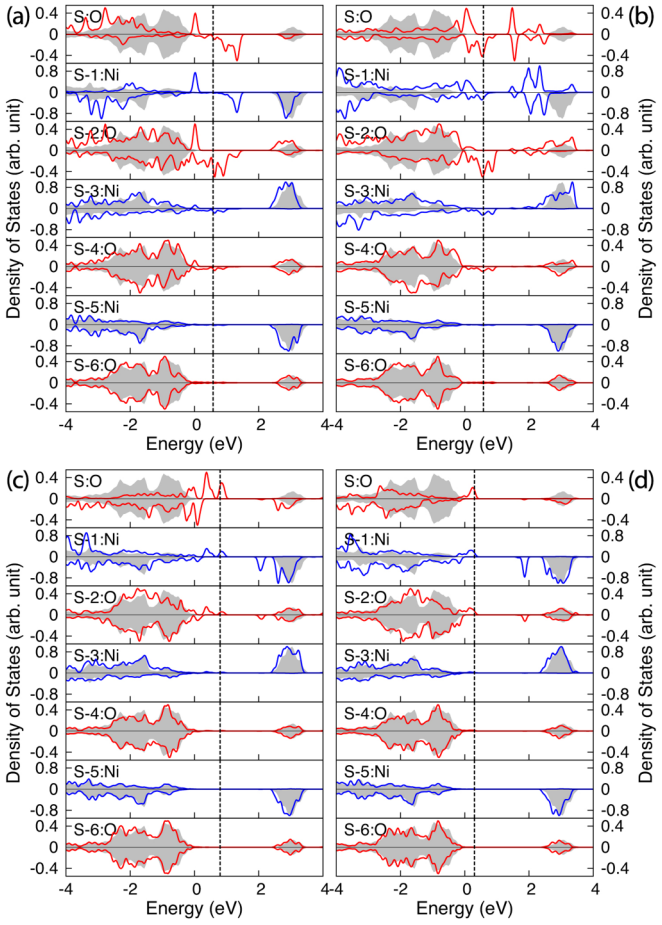

FIG. 6. (Color online) Layer-resolved PDOS comparison between bulk NiO and (a) Rt3_Ni, (b) Rt3_Ni-H, (c) Rt3_O, (d) Rt3_O-H surface structures. VBM of bulk NiO is set to 0, Fermi levels of different reconstructed surfaces are shown in dashed line. The Ni-3d and O-2p PDOS are represented by blue and red lines, and the bulk NiO PDOS is shown in solid gray.

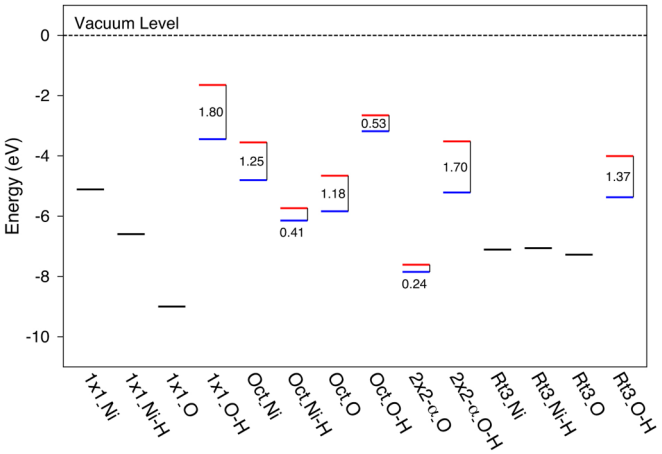

FIG. 7. (Color online) Calculated band positions of studied NiO(111) reconstructed surfaces. The lower edge of the conduction band (red) and upper edge of the valence band (blue) are presented along with the band gap in electron volts. The calculated Fermi levels of the surface structures with metallic property such as 1×1_Ni, 1×1_Ni − H, 1×1_O, Rt3_Ni, Rt3_Ni-H, and Rt3_O are also depicted.

not only the energy gap type and magnitude but also the relative energy levels alignment (with respect to the vacuum) varies considerably among all these reconstructed surfaces of NiO(111). Hydroxylated passivation appears to result in the highest HOMO energy for all these reconstructed surfaces, and this is likely to be important for the application of NiO as a p-type material under ambient conditions. For 1×1 and Rt3 reconstructions, the hydroxylated surface is the only one that shows an insulating character. Because some of the reconstructed NiO(111) surfaces possess a small energy gap (even show the metallic character) due to the presence of surface states within the band gap, phonon-mediated electron-hole recombination is likely to negatively influence the device performance in context of p-DSSC/p-DSPEC applications.

IV. CONCLUSIONS

We presented a systematic study of how the surface reconstruction and passivation influence the antiferromagnetic and electronic structures of the NiO(111) surface using electronic structure calculations. These features lead to a surprisingly wide variety of different surface electronic structures, and some surfaces are even metallic. Meanwhile, the antiferromagnetic character of bulk NiO in the ⟨111⟩ direction is retained even near the surface, and the magnetic moment quickly converges to the bulk value within a few surface layers. More specifically, Oct_Ni, Oct_O, and 2×2-α_O-H surfaces are found to be charge-transfer type insulators with significant contribution of the VBM and CBM from O-2p states and Ni-3d states, respectively. At the same time, the 2×2-α_O surface shows the insulating energy gap of O-2p character at both band edges, and the Oct_O-H surface shows a Mott-type gap with both band edges of Ni-3d character. Oct_Ni-H surface exhibits a hybridized band gap [69,70] where the VBM is contributed almost equally from O-2p and Ni-3d states, and the CBM is of Ni-3d character. Interestingly, ideal 1×1 surfaces and Rt3 reconstructed surfaces are metallic unless they are hydroxylated. The 1×1_O-H surface shows an insulating energy gap with significant contribution of the VBM and CBM from O-2p orbitals and hydrogen s orbital, respectively. The Rt3_O-H surface, however, shows a charge-transfer-type energy gap with significant contribution of the VBM and CBM from O-2p and Ni-3d states, respectively.

ACKNOWLEDGMENTS

This work was wholly funded by the UNC Energy Frontier Research Center (EFRC) “Center for Solar Fuels”, an EFRC funded by the U.S. Department of Energy, Office of Science, Office of Basic Energy Sciences, under Award DE-SC0001011.

APPENDIX A: EFFECT OF HUBBARD U ON ELECTRONIC STRUCTURE

Figure 8 shows that Hubbard-U correction increases the band gap dramatically from 1.49–3.38 eV when the U parameter is varied from 0 (DFT calculation without Hubbard-U correction) to 8.0 eV. An important feature of GGA + U calculations is that nature of the states at the top of the valence band is qualitatively changed, and hence the nature

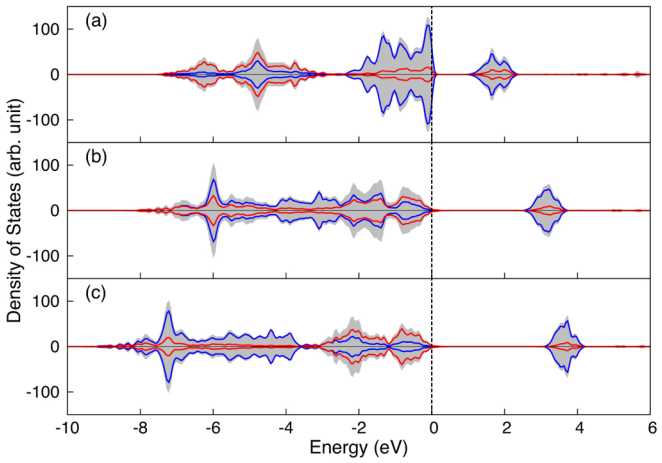

FIG. 8. (Color online) Spin-resolved PDOS (spin up PDOS with positive values, spin down PDOS with negative values) for Ni-3d (blue line), O-2p (red line) orbitals, and total DOS (gray solid) of bulk NiO within (a) DFT, (b) DFT+U with $U = 5.4$ eV, (c) DFT + U with $U = 8.0$ eV. VBM is set to 0 and shown in dashed line.

of the band gap. In GGA calculations the top of valence band is mainly dominated by Ni-3d electrons; on the other hand, in the GGA + U calculations the O-2p electrons give the most important contribution to the top of valence band. Both GGA and GGA + U calculations show that the bottom of the conduction band is mostly of Ni-3d states. Thus, the enhancement of the O-2p character near the top of valence band with the Hubbard correction leads to the change of the insulating band gap character from Mott-Hubbard-type (GGA calculations) to charge-transfer-type (GGA + U calculations), which agrees well with the findings in previous works, both experimentally and theoretically [51,54–56,61–65]. Although our calculation using the linear response approach [51,57] gives 4.45 eV for the value of U, we used the value of 5.4 eV in this work so that our work can be compared to previous theoretical works which use 5.4 eV for the U value [37,42,56,66,67]. We observe that our choice of 4.45 eV or 5.4 eV for the U parameter does not significantly influence the electronic structure including the magnetic moment and energy gap type.

APPENDIX B: SUPERCELL OF DIFFERENT RECONSTRUCTED NiO(111) SURFACES

Figure 9 shows all the supercell structures (top and side view) of the different reconstructed NiO(111) surfaces studied in this work.

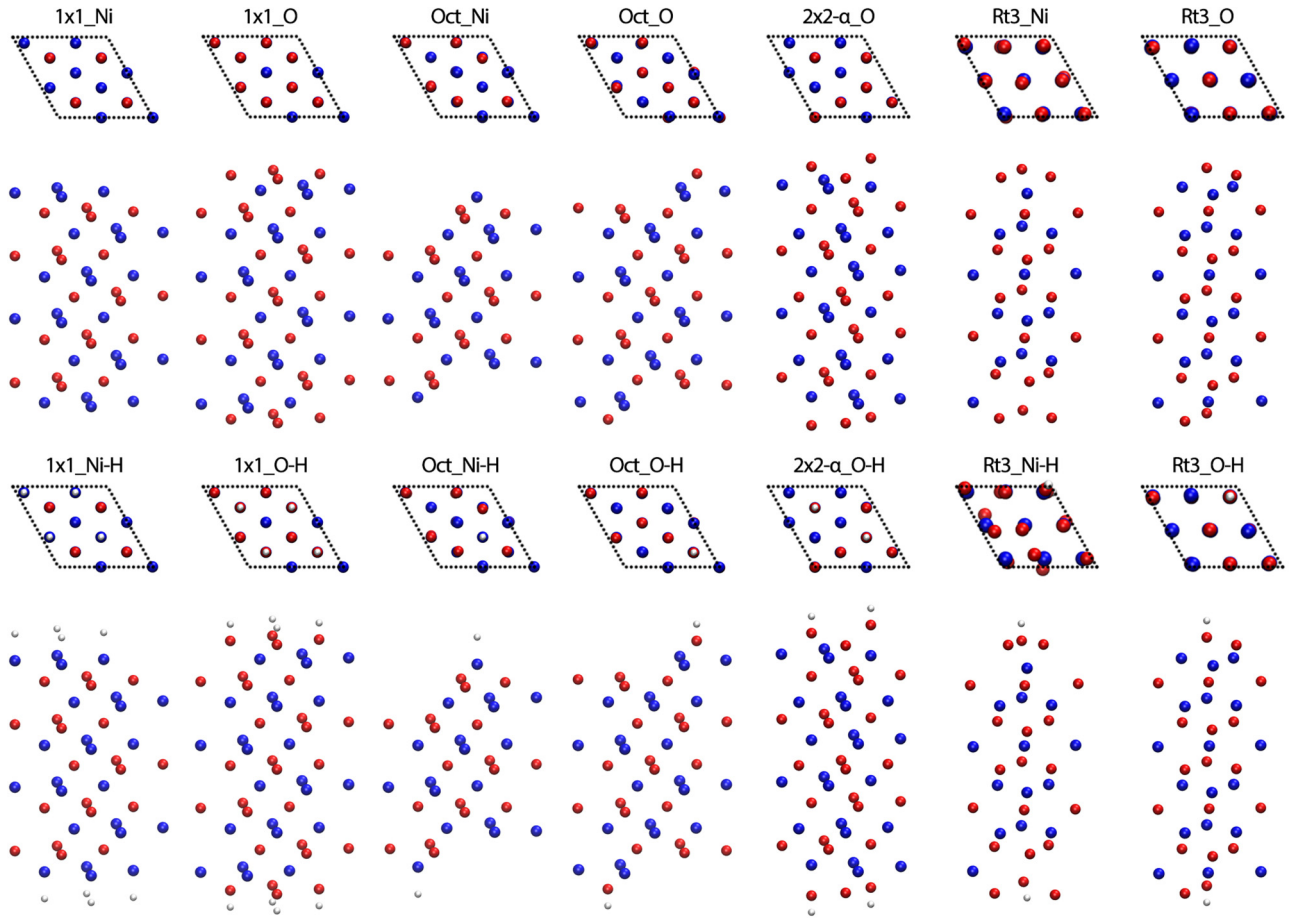

FIG. 9. (Color online) Top and side view of the super cells used in our calculations for 1×1_Ni, 1×1_O, Oct_Ni, Oct_O, 2×2-α_O, Rt3_Ni, and Rt3_O surface models, as well as their hydrogenated/hydroxylated counterparts. Red and blue balls represent oxygen and nickel atoms, and hydrogen atoms are shown in white.

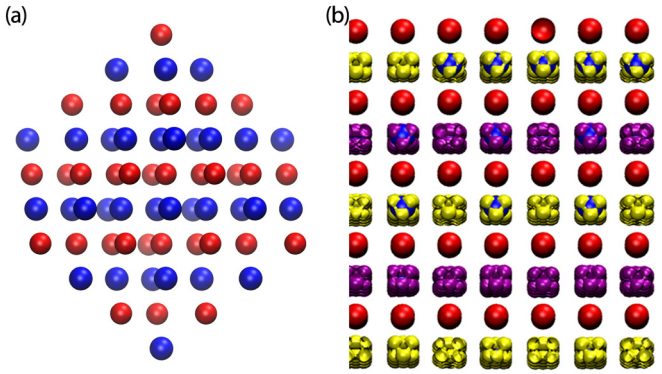

FIG. 10. (Color online) Side view of (a) the super cell and (b) the calculated magnetization density $m(x) = \rho_{\uparrow}(x) - \rho_{\downarrow}(x)$ of bulk NiO. Red and blue balls represent oxygen and nickel atoms. Yellow and purple isosurfaces indicate spin-up and spin-down density, respectively.

APPENDIX C: SUPERCELL AND MAGNETIZATION OF BULK NiO

Figure 10 shows the supercell and the calculated magnetization of bulk NiO.

TABLE II. Summarize of magnetic and electronic properties for Oct_O slabs with six, eight, and ten layers of nickel. *S*: surface layer; *S-N*: the *N*th layer below top surface.

Structures		Bulk	Oct_O_6	Oct_O_8	Oct_O_10
Thickness/nm		n/a	1.43	1.92	2.41
Energy Gap/eV		2.43	1.18	1.19	1.19
Gap Type		CT	CT	CT	CT
Magnetic Momentum/μ_B	*S*	0.00	0.22	0.22	0.22
	S-1	1.59	1.61	1.61	1.61
	S-2	0.00	0.02	0.02	0.02
	S-3	−1.59	−1.60	−1.60	−1.59

APPENDIX D: THICKNESS DEPENDENCE ON THE ELECTRONIC AND MAGNETIC PROPERTY

Table II summarizes the calculated electronic and magnetic properties as a function of the slab thickness for octopolar surface. Our DFT + U calculation shows that both electronic and magnetic properties of NiO(111) surface are well converged even for the slab with six layers of nickel.

[1] R. M. Gabr, A. N. El-Naimi, and M. G. Al-Thani, Thermochim. Acta **197**, 307 (1992).
[2] M. Yoshio, Y. Todorov, K. Yamato, H. Noguchi, J.-i. Itoh, M. Okada, and T. Mouri, J. Power Sources **74**, 46 (1998).
[3] S. Ikeda, T. Takata, M. Komoda, M. Hara, J. N. Kondo, K. Domen, A. Tanaka, H. Hosono, and H. Kawazoe, Phys. Chem. Chem. Phys. **1**, 4485 (1999).
[4] H. Steinebach, S. Kannan, L. Rieth, and F. Solzbacher, Sensors and Actuators B (Chemical) **151**, 162 (2010).
[5] A. C. Sonavane, A. I. Inamdar, P. S. Shinde, H. P. Deshmukh, R. S. Patil, and P. S. Patil, J. Alloys Compd. **489**, 667 (2010).
[6] J. Park *et al.*, Adv. Mater. **17**, 429 (2005).
[7] W. L. Roth, Phys. Rev. **110**, 1333 (1958).
[8] L. Neel, in *Low Temperature Physics*, edited by C. DeWitt, B. Dreyfus, and P. de Gennes (Gordon and Breach, New York, 1962), p. 235.
[9] R. H. Kodama, S. A. Makhlouf, and A. E. Berkowitz, Phys. Rev. Lett. **79**, 1393 (1997).
[10] C. R. H. Bahl, M. F. Hansen, T. Pedersen, S. Saadi, K. H. Nielsen, B. Lebech, and S. Mørup, J. Phys.: Condens. Matter **18**, 4161 (2006).
[11] J. B. Yi, J. Ding, Y. P. Feng, G. W. Peng, G. M. Chow, Y. Kawazoe, B. H. Liu, J. H. Yin, and S. Thongmee, Phys. Rev. B **76**, 224402 (2007).
[12] M. Jagodič, Z. Jagličić, A. Jelen, J. B. Lee, Y.-M. Kim, H. J. Kim, and J. Dolinšek, J. Phys.: Condens. Matter **21**, 215302 (2009).
[13] M. P. Proenca, C. T. Sousa, A. M. Pereira, P. B. Tavares, J. Ventura, M. Vazquez, and J. P. Araujo, Phys. Chem. Chem. Phys. **13**, 9561 (2011).
[14] N. Rinaldi-Montes *et al.*, Nanoscale **6**, 457 (2014).
[15] J. Nogués and I. K. Schuller, J. Magn. Magn. Mater. **192**, 203 (1999).
[16] U. Bach, D. Lupo, P. Comte, J. E. Moser, F. Weissortel, J. Salbeck, H. Spreitzer, and M. Gratzel, Nature (London) **395**, 583 (1998).
[17] A. Hagfeldt and M. Grätzel, Acc. Chem. Res. **33**, 269 (2000).
[18] M. Gratzel, Nature (London) **414**, 338 (2001).
[19] L. Alibabaei *et al.*, Proc. Natl. Acad. Sci. USA **110**, 20008 (2013).
[20] L. Alibabaei, H. Luo, R. L. House, P. G. Hoertz, R. Lopez, and T. J. Meyer, J. Mater. Chem. A **1**, 4133 (2013).
[21] J. He, H. Lindström, A. Hagfeldt, and S.-E. Lindquist, J. Phys. Chem. B **103**, 8940 (1999).
[22] E. A. Gibson *et al.*, Angew. Chem. **48**, 4402 (2009).
[23] F. Odobel, L. Le Pleux, Y. Pellegrin, and E. Blart, Acc. Chem. Res. **43**, 1063 (2010).
[24] J. J. Concepcion, R. L. House, J. M. Papanikolas, and T. J. Meyer, Proc. Natl. Acad. Sci. USA **109**, 15560 (2012).
[25] F. Odobel and Y. Pellegrin, J. Phys. Chem. Lett. **4**, 2551 (2013).
[26] J. He, H. Lindström, A. Hagfeldt, and S.-E. Lindquist, Sol. Energ. Mater. Sol. Cells **62**, 265 (2000).
[27] A. Nattestad, A. J. Mozer, M. K. R. Fischer, Y. B. Cheng, A. Mishra, P. Bauerle, and U. Bach, Nat. Mater. **9**, 31 (2010).
[28] S. Powar *et al.*, Angew. Chem. **52**, 602 (2013).
[29] C. E. Castillo *et al.*, J. Phys. Chem. C **119**, 5806 (2015).
[30] Z. Huang, G. Natu, Z. Ji, M. He, M. Yu, and Y. Wu, J. Phys. Chem. C **116**, 26239 (2012).
[31] F. Odobel, Y. Pellegrin, E. A. Gibson, A. Hagfeldt, A. L. Smeigh, and L. Hammarström, Coord. Chem. Rev. **256**, 2414 (2012).

[32] C. J. Flynn, E. E. Oh, S. M. McCullough, R. W. Call, C. L. Donley, R. Lopez, and J. F. Cahoon, J. Phys. Chem. C **118**, 14177 (2014).
[33] D. Wolf, Phys. Rev. Lett. **68**, 3315 (1992).
[34] A. Barbier, C. Mocuta, H. Kuhlenbeck, K. F. Peters, B. Richter, and G. Renaud, Phys. Rev. Lett. **84**, 2897 (2000).
[35] N. Erdman, O. Warschkow, D. E. Ellis, and L. D. Marks, Surf. Sci. **470**, 1 (2000).
[36] A. Subramanian, L. D. Marks, O. Warschkow, and D. E. Ellis, Phys. Rev. Lett. **92**, 026101 (2004).
[37] W.-B. Zhang and B.-Y. Tang, J. Chem. Phys. **128**, 124703 (2008).
[38] J. Ciston, A. Subramanian, and L. D. Marks, Phys. Rev. B **79**, 085421 (2009).
[39] J. Ciston, A. Subramanian, D. M. Kienzle, and L. D. Marks, Surf. Sci. **604**, 155 (2010).
[40] P. W. Tasker, J. Phys. C **12**, 4977 (1979).
[41] P. M. Oliver, S. C. Parker, and W. C. Mackrodt, Model. Simul. Mater. Sci. Eng. **1**, 755 (1993).
[42] O. Bengone, M. Alouani, J. Hugel, and P. Blöchl, Comput. Mater. Sci. **24**, 192 (2002).
[43] C. A. J. Fisher, Scr. Mater. **50**, 1045 (2004).
[44] S. Wang, S. Liu, J. Guo, K. Wu, and Q. Guo, Surf. Sci. **606**, 378 (2012).
[45] P. Giannozzi *et al.*, J. Phys.: Condens. Matter **21**, 395502 (2009).
[46] H. J. Monkhorst and J. D. Pack, Phys. Rev. B **13**, 5188 (1976).
[47] K. Terakura, T. Oguchi, A. R. Williams, and J. Kübler, Phys. Rev. B **30**, 4734 (1984).
[48] V. I. Anisimov, J. Zaanen, and O. K. Andersen, Phys. Rev. B **44**, 943 (1991).
[49] V. I. Anisimov, I. V. Solovyev, M. A. Korotin, M. T. Czyżyk, and G. A. Sawatzky, Phys. Rev. B **48**, 16929 (1993).
[50] A. I. Liechtenstein, V. I. Anisimov, and J. Zaanen, Phys. Rev. B **52**, R5467 (1995).
[51] M. Cococcioni and S. de Gironcoli, Phys. Rev. B **71**, 035105 (2005).
[52] J. P. Perdew, K. Burke, and M. Ernzerhof, Phys. Rev. Lett. **77**, 3865 (1996).
[53] S. L. Dudarev, G. A. Botton, S. Y. Savrasov, C. J. Humphreys, and A. P. Sutton, Phys. Rev. B **57**, 1505 (1998).
[54] F. Tran, P. Blaha, K. Schwarz, and P. Novák, Phys. Rev. B **74**, 155108 (2006).
[55] Pan Wei and Z. Q. Qi, Phys. Rev. B **49**, 10864 (1994).
[56] O. Bengone, M. Alouani, P. Blöchl, and J. Hugel, Phys. Rev. B **62**, 16392 (2000).
[57] W. E. Pickett, S. C. Erwin, and E. C. Ethridge, Phys. Rev. B **58**, 1201 (1998).
[58] F. Aryasetiawan, K. Karlsson, O. Jepsen, and U. Schönberger, Phys. Rev. B **74**, 125106 (2006).
[59] T. Miyake and F. Aryasetiawan, Phys. Rev. B **77**, 085122 (2008).
[60] B. H. Brandow, Adv. Phys. **26**, 651 (1977).
[61] G. A. Sawatzky and J. W. Allen, Phys. Rev. Lett. **53**, 2339 (1984).
[62] G. Lee and S. J. Oh, Phys. Rev. B **43**, 14674 (1991).
[63] O. Tjernberg, S. Söderholm, U. O. Karlsson, G. Chiaia, M. Qvarford, H. Nylén, and I. Lindau, Phys. Rev. B **53**, 10372 (1996).
[64] M. R. Castell, S. L. Dudarev, G. A. D. Briggs, and A. P. Sutton, Phys. Rev. B **59**, 7342 (1999).
[65] H. Jiang, R. I. Gomez-Abal, P. Rinke, and M. Scheffler, Phys. Rev. B **82**, 045108 (2010).
[66] A. Rohrbach, J. Hafner, and G. Kresse, Phys. Rev. B **69**, 075413 (2004).
[67] C. Ebensperger and B. Meyer, Physica Status Solidi B **248**, 2229 (2011).
[68] F. Finocchi, A. Barbier, J. Jupille, and C. Noguera, Phys. Rev. Lett. **92**, 136101 (2004).
[69] J. Zaanen, G. A. Sawatzky, and J. W. Allen, Phys. Rev. Lett. **55**, 418 (1985).
[70] T. M. Schuler, D. L. Ederer, S. Itza-Ortiz, G. T. Woods, T. A. Callcott, and J. C. Woicik, Phys. Rev. B **71**, 115113 (2005).